This is the accepted manuscript made available via CHORUS. The article has been published as:

Interfacial geometry in particle-forming phases of diblock copolymers

Ryan P. Collanton and Kevin D. Dorfman

Phys. Rev. Materials **6**, 015602 — Published 14 January 2022

DOI: 10.1103/PhysRevMaterials.6.015602

Interfacial Geometry in Particle-Forming Phases of Diblock Copolymers

Ryan P. Collanton and Kevin D. Dorfman*

Department of Chemical Engineering and Materials Science,

University of Minnesota–Twin Cities,

421 Washington Ave. SE, Minneapolis, MN 55455

(Dated: December 23, 2021)

Abstract

Frank-Kasper (FK) phases are complex particle packings known to form in a wide variety of hard and soft materials, including single-component AB diblock copolymer melts. An important open question in the context of this system is why these lower-symmetry packings are selected over the classical, higher-symmetry, body-centered cubic phase. To address this question, we simulated a library of diblock copolymer melts under intermediate-segregation conditions using self-consistent field theory and performed a combination of geometric and thermodynamic analyses. Our findings show that imprinting of the enclosing Voronoi polyhedra onto the micelle core is generally weak, but nonetheless coincides with sharpening of the interface between A and B monomers compared to more spherical cores. The corresponding reduction in enthalpy, which is the dominant contribution to the free energy, drives the bcc-σ transition, overcoming increases in stretching penalties and giving way to more polyhedral micelle cores. These results offer insight into the stability and formation of Frank-Kasper phases under experimentally realistic conditions.

I. INTRODUCTION

Block copolymers, a class of soft matter consisting of distinct polymer chains chemically linked together, offer exceptional tunability and a massive design space, making them strong candidates for the pursuit of novel soft materials [1]. Due to thermodynamic incompatibility of the chemically distinct blocks and their inability to macroscopically separate, block copolymers undergo spontaneous self-assembly below their order-disorder temperature (ODT) into crystalline phases with nanoscale ordering [2]. The selection of the system's equilibrium phase is controlled via the polymer's molecular architecture and chemical composition. In the particle-forming region of the resulting phase space, block copolymers assemble into quasi-spherical, micelle-like particles [3–5]. These particles pack to fill space at constant density, and the structure and symmetry of the resulting packings, such as those in Fig. 1, controls material physical properties, analogous to molecular packing in hard materials [6, 7]. Because of this structure-property relationship and the potential to leverage it to control material properties, it is of interest to understand the driving forces leading to specific point-packings of these soft, deformable micellar particles.

* dorfman@umn.edu

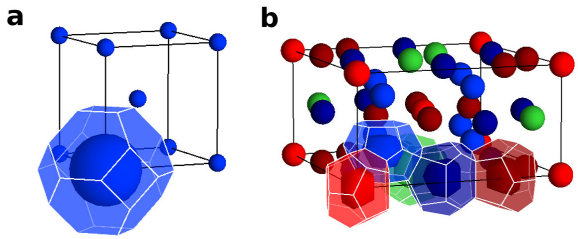


FIG. 1. A schematic depiction of the point-packings for (a) bcc and (b) σ. The particle coloring represents different Wyckoff positions. One Voronoi polyhedron is shown per Wyckoff position. Particle cores are depicted as spherical in bcc and polyhedral in σ [7].

Diblock copolymers are a specific type of block copolymer composed of two blocks of distinct monomers (A and B) linked at a single junction. In the mean-field approximation, the phase behavior of linear, Gaussian diblock copolymers can be fully described via three molecular parameters, defined using a common reference volume [8]. First, the relative lengths of the A and B blocks are quantified by the block fraction $f_{\mathrm{A}} = N_{\mathrm{A}}/N$, where N_i is the degree of polymerization of the block with monomer type i and $N = N_{\mathrm{A}} + N_{\mathrm{B}}$ is the total degree of polymerization [9]. Second, the conformational asymmetry $\epsilon = b_{\mathrm{A}}/b_{\mathrm{B}}$ describes the relative elasticity of the A and B blocks, where b_i is the statistical segment length of monomer type i. Because entropic stretching energy for a Gaussian coil scales like b_i^{-2} [8], increasing ϵ leads to stiffer B blocks and more flexible A blocks. Finally, the segregation strength χN describes the strength of repulsive interactions between A and B monomers, where χ is the Flory-Huggins interaction parameter [10]. By setting the trio $(f_{\mathrm{A}}, \epsilon, \chi N)$, the thermodynamics of the system are fully specified in the mean-field limit. Given their simplicity and strong theoretical foundation, diblock copolymers offer an ideal model system for studying self-assembly in soft-matter systems.

Even within such a simple framework, the design space exhibited by diblock copolymers is surprisingly large. A wide array of ordered phases have been observed experimentally, including the classical phases of lamellae [11], hexagonal cylinders (hex) [11], close-packed spheres [12–14], and body-centered cubic (bcc) spheres [11] (Fig 1a); the network phases O^{70} [15, 16] and double-gyroid (DG) [17, 18]; and the Frank-Kasper (FK) phases σ [19, 20] (Fig 1b) and A15 [21]. Experimental discovery has often been led by theoretical and computational efforts to map the phase space of diblock copolymers and predict order-order

transitions (OOTs) [22, 23].

The primary focus of this study is on the particle-forming phases that emerge in compositionally asymmetric diblock systems. We define A to be the minority block ($f_A < 0.50$) such that A blocks comprise the micelle core while B blocks constitute the corona. In a sea of corona homopolymer, a single micelle would tend to be spherical, but under the aforementioned packing constraints, the micelles must deform to fill space at uniform density [6]. The resulting internal micelle structure, which neither perfectly replicates that of the enclosing Voronoi (Wigner-Seitz) cell nor is perfectly spherical [24], arises from a thermodynamic balance of entropic chain stretching and enthalpic interaction penalties [25].

It is desirable to rationalize Frank-Kasper phase thermodynamics through intuitive arguments pertaining to the geometry of the constituent polymer micelles. Though an intuitive understanding of the driving forces leading to particular geometries and phase equilibria has remained elusive [26], there have been two significant steps towards this end [6, 27]. In the first, Lee *et al.* [6] highlighted a contrast between global lattice symmetry (i.e., the number of general equivalent positions, GEPs, in the space group) and local particle sphericity (i.e., the shapes of the micelles). The σ lattice exhibits significantly lower symmetry (16 GEPs) than the bcc lattice (96 GEPs) [28]. Invoking the maxim that nature tends toward high-symmetry states, they hypothesized that the order-order transition from bcc to σ results from the higher mean sphericity of the Voronoi cells in σ relative to those in bcc, alluding to a trade-off between global lattice symmetry and local particle sphericity. Intriguingly, they also drew connections between intermetallic and block polymer systems, suggesting a relationship between the importance of sphericity in real space for polymers and reciprocal space for metals. Though beautiful in its simplicity and a pioneering step towards understanding the bcc-σ phase transition, this study does not provide any insight into the underlying polymer physics leading to the observed phenomena, and begs the question as to what particular effects drive block polymer micelle packings towards different symmetries.

Progress has also been made rationalizing polymer micelle geometry and justifying the bcc-σ OOT in the strong-segregation ($\chi N \to \infty$) limit. In this limit, the A/B interface is infinitely sharp, and the dominant contribution to the enthalpy is at the dividing surface between the pure A and B regions [29, 30]. The enthalpy is thus directly controlled by the area of this dividing surface (the interface), simplifying the free energy optimization to a balance of interfacial area and chain stretching. In the second major step, Reddy *et al.*

[27] investigated particle-forming phases using a diblock foam model [29, 30] in the strong-segregation and polyhedral interface limits, where the shape of the polyhedral boundary is perfectly imprinted onto sharp A/B interfaces, enabling free energy calculation via purely geometric measures. Permitting mass exchange and shape relaxation in the diblock foam, they demonstrated that although σ offers neither the optimal interfacial area nor optimal chain stretching, it offers the best compromise between the two. The authors also briefly investigated the extent of polyhedral imprinting of the Voronoi polyhedra onto the A/B interface in the infinite chain ($N \to \infty$) limit using self-consistent field theory (SCFT); they reported clear distinctions between the bcc and A15 phases, but did not examine other known phases or connect these features to free energy or stability.

In this study, we answer a number of open questions regarding the geometry and stability of diblock copolymer phases in the intermediate-segregation particle-forming regime that follow from the aforementioned studies by Lee *et al.* [6] and Reddy *et al.* [27]. First, we clarify the relationship of the geometry of polymer micelles with the three polymer system parameters ($f_{\mathrm{A}}, \epsilon, \chi N$). We then examine the bcc-σ transition, and address the consistent relationship between micelle geometry and phase stability across phase space, hinted at by the schematic depictions of the micelle cores in Fig. 1. Finally, we examine enthalpic and entropic contributions to the free energy and illuminate the primary driving force, along with its structural manifestation, for the phase transition from bcc to σ in the mean-field approximation.

II. METHODOLOGY

A. Self-Consistent Field Theory

The properties of diblock copolymer melts were computed in the mean-field limit via variable unit cell self-consistent field theory (SCFT), as implemented in the open-source package Polymer Self-Consistent Field (PSCF) [31, 32]. The modified diffusion equations (MDEs) describe the configuration of a continuous Gaussian chain of length N in an external

field [33],

$$\frac{\partial}{\partial s}q(\mathbf{r},s) = \frac{b_{i(s)}^2}{6}\,\nabla^2 q(\mathbf{r},s) - \omega_{i(s)}(\mathbf{r})\,q(\mathbf{r},s) \tag{1}$$

$$-\frac{\partial}{\partial s}q^\dagger(\mathbf{r},s) = \frac{b_{i(s)}^2}{6}\,\nabla^2 q^\dagger(\mathbf{r},s) - \omega_{i(s)}(\mathbf{r})\,q^\dagger(\mathbf{r},s), \tag{2}$$

subject to the inital conditions

$$q(\mathbf{r},0) = q^\dagger(\mathbf{r},N) = 1, \tag{3}$$

where chain propagator $q(\mathbf{r},s)$ is the statistical weight of a chain of length s terminating at position $\mathbf{r}$ under the external potential field $\omega_{i(s)}$ propagated from segment 0 to s. The complementary backwards chain propagator $q^\dagger(\mathbf{r},s)$ is the statistical weight of a chain of length $N-s$ propagated along the chain from segment N to s. The function $i(s)$ indicates the monomer type at segment s such that $\omega_{i(s)}$ describes the field acting on monomer type $i(s)$. The single-chain partition function Q is given by

$$Q = \frac{1}{V}\int \mathrm{d}\mathbf{r}\; q(\mathbf{r},N), \tag{4}$$

where V is the volume of the unit cell. In SCFT, the interactions of polymer segments with other segments are represented as a spatially-varying chemical potential field. The chemical potential field is both generated and experienced by the segments, giving rise to the self-consistent nature of the solution. To accomplish this, first the monomer volume fraction field $\phi_i(\mathbf{r})$ is computed via

$$\phi_i(\mathbf{r}) = \frac{1}{NQ}\int_i ds\; q(\mathbf{r},s)\,q^\dagger(\mathbf{r},s), \tag{5}$$

where the integral is over the segments on the chain of monomer type i and the volume fractions are subject to an incompressibility constraint $\sum_\alpha \phi_\alpha(\mathbf{r}) = 1$. The chemical potential fields $\omega_i(\mathbf{r})$ experienced by monomer types i at position $\mathbf{r}$ due to nearby segments are then directly calculated as

$$\omega_A(\mathbf{r}) = \chi\,\phi_B(\mathbf{r}) + \xi(\mathbf{r}) \tag{6}$$

$$\omega_B(\mathbf{r}) = \chi\,\phi_A(\mathbf{r}) + \xi(\mathbf{r}), \tag{7}$$

where $\xi(\mathbf{r})$ is a Lagrange multiplier pressure field enforcing incompressibility. Equations (1)-(7) are solved self-consistently for the unknown chemical potential fields. This process is

done iteratively by first inputting initial guesses for $\omega_i(\mathbf{r})$, solving the MDEs in Eqs. (1)-(3), calculating the volume fraction fields with Eq. (5), and calculating the chemical potential fields generated by the polymer segments with Eqs. (6)-(7). Then, the resulting chemical potential fields are compared with the guesses inputted to the MDEs. If they are similar enough, the iterative loop ends; otherwise, the guesses for the fields are updated and the process starts over. The SCFT calculations for this study were performed using a Newton-Raphson field update scheme [31] for the A15, bcc, fcc, and hex phases and an Anderson Mixing update scheme [34] for the σ phase, where the large unit cell causes memory issues in the Newton-Raphson method. Calculations using Newton-Raphson were done with a Jacobian cutoff-size of 100 elements. Calculations using Anderson Mixing combined 20 histories with a mixing parameter λ ramping up from zero with successive iterations and capped at unity when the number of iterations exceeds the number of histories, as described by Stasiak and Matsen [35].

The key outputs of each SCFT calculation are the Helmholtz free energy and the spatial volume fraction fields $\phi_{\mathrm{A}}(\mathbf{r})$ and $\phi_{\mathrm{B}}(\mathbf{r}) = 1 - \phi_{\mathrm{A}}(\mathbf{r})$. The Helmholtz free energy per monomer reference volume F, identical to the Gibbs free energy due to the incompressibility constraint, is given by

$$\frac{F}{k_{\mathrm{B}}T} = -\frac{1}{N}(\ln Q + 1) - \frac{1}{V}\int \mathrm{d}\mathbf{r}\; \omega_{\mathrm{A}}(\mathbf{r})\,\phi_{\mathrm{A}}(\mathbf{r}) - \frac{1}{V}\int \mathrm{d}\mathbf{r}\; \omega_{\mathrm{B}}(\mathbf{r})\,\phi_{\mathrm{B}}(\mathbf{r}) + \frac{\chi}{V}\int \mathrm{d}\mathbf{r}\; \phi_{\mathrm{A}}(\mathbf{r})\,\phi_{\mathrm{B}}(\mathbf{r}), \quad (8)$$

where the integrals are performed over the unit cell. The volume fraction fields are expressed as an expansion in terms of symmetry-adapted basis functions that satisfy the corresponding space group's symmetry operations, constituting a pseudo-spectral solution to the MDEs [35–37].

A15 structures were spatially resolved with a grid of size 36×36×36, fcc with 36×36×36, bcc with 48×48×48, σ with 128×128×64, and hex with 64×64. These grid sizes were selected based on Ref. 38. All calculations were done with a contour step size $ds = 10^{-2}$. Error was calculated as the maximum of the stress and the residuals of the self-consistent field equations, and the criterion for convergence was an error tolerance of 10^{-5} [32]. SCFT data produced by Kim *et al.* [38] were used as initial guesses for the calculations. Diblock polymer parameters f_{A}, ϵ, and χN were varied using PSCF's parameter sweep function, where $\epsilon = b_{\mathrm{A}}/b_{\mathrm{B}}$ was varied by fixing $b_{\mathrm{B}} = 1$ and increasing b_{A}. The region of phase space

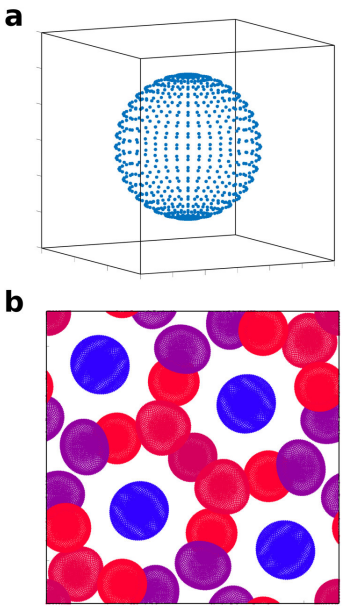


FIG. 2. Point clouds on the $\phi_{\mathrm{A}}(\mathbf{r}) = 0.50$ volume fraction isosurfaces of (a) a toy model of a perfectly spherical micelle core, and (b) a diblock copolymer σ phase computed via SCFT. For (b), the unit cell is viewed along the [001] direction, and particles are colored on a spectrum from blue (low sphericity) to red (high sphericity). Asphericity is clearly exhibited by the purple particles (Wyckoff position 8i′) in Z14 Voronoi polyhedra (14 faces).

explored included $\epsilon = 1.5, 1.6, \ldots, 2.0$ and $\chi N = 20, 21, \ldots, 30$, with a range of f_{A} to fully cover the particle-forming region at each ϵ and χN.

B. Geometric Post-Processing

Particle core geometry was numerically mapped using a root-finding algorithm developed for this study. First, the symmetry-adapted Fourier representations of the volume fraction fields outputted by PSCF were converted to a real space coordinate grid representation using the functionality built into PSCF. Then, the basis set and general equivalent positions of each phase were used to calcate particle center coordinates [28, 39]. For each particle, a series of root-finding problems along rays emitting from the particle center were solved to identify points where $\phi_{\mathrm{A}} = \phi_{\mathrm{B}} = 0.50$. To facilitate this task, gridded volume fraction fields were interpolated using three-dimensional spline interpolation. Rays emitting from the particle center were spaced evenly on a grid of the polar and azimuthal angles with spacing 0.02π.

Per particle, 4951 points were identified to form a point cloud on the 50% volume fraction isosurface, as depicted in Fig. 2. Erroneous points, likely due to accumulation of numerical error, were determined as any point with a distance from its corresponding particle center greater than four scaled median absolute deviations away from a 1238-point (i.e. a quarter of the total points per particle) moving median. Post-processed calculations with one or more erroneous points on any particle were flagged and omitted from further data analyses. Only three such structures were identified out of a total of just under 20,000 total polymer structures simulated.

Further geometric analysis of individual particles was performed to quantify the shapes of the polymer micelle core relative to the Voronoi (Wigner-Seitz) cell polyhedra. First, the convex hull of the point cloud on the particle core isosurface was computed. Additionally, the hull's enclosed volume and surface triangulation were found, enabling facile calculation of the particle core surface area via summation. Measures of core geometry such as the isoperimetric quotient (IQ) [6, 40] and imprinting order parameter (α) [27] were then computed using the surface areas and enclosed volumes. Isoperimetric quotient describes the sphericity of an arbitrary shape of volume V and area A, and is defined as

$$\mathrm{IQ} = \frac{36\pi V^2}{A^3}, \tag{9}$$

with limits of zero for a flat sheet and unity for a sphere. The imprinting order parameter, as introduced by Reddy *et al.* [27], describes the extent to which a shape has deformed from a sphere towards a specific polyhedron. It is defined as

$$\alpha = \frac{1 - \mathrm{IQ}^{-1/3}}{1 - \mathrm{IQ}_{\mathrm{poly}}^{-1/3}}, \tag{10}$$

where $\mathrm{IQ}^{-1/3} = A/(36\pi V^2)^{1/3}$ is the dimensionless area, with the denominator corresponding to the area the shape would have if it maintained its volume but was perfectly spherical. The imprinting parameter has convenient limits of zero for a perfectly spherical shape ($\mathrm{IQ} = 1$) and unity for a fully imprinted, perfectly polyhedral shape ($\mathrm{IQ} = \mathrm{IQ}_{\mathrm{poly}}$). The performance of this numerical geometric algorithm was benchmarked by analyzing toy models of known geometries, including a perfect sphere and Voronoi cell polyhedra, and comparing the numerical output to the correct answer. Performance of the algorithm was determined to be more accurate for more spherical geometries and less accurate for less spherical geometries, but

accurate enough in either case to discern geometric differences and identify trends. Details of this validation are available in the Supplemental Material (SM) [41].

To aggregate particle imprinting and sphericity data into quantitative metrics useful for comparison between distinct phases, volume-weighted averages of single-particle metrics were computed. For example, the volume-weighted average of α for a single SCFT result is given by

$$\langle \alpha \rangle_V = \frac{\sum_i V_i \alpha_i}{\sum_i V_i}, \tag{11}$$

where the sums are over all particles in the unit cell. Volume-weighted averages were chosen over number averages as an attempt to account for the higher contribution to the free energy of larger particles. The corresponding code used for all numerical post-processing is available on GitHub [42].

III. POLYMER MICELLE GEOMETRY ACROSS PHASE SPACE

To begin the investigation into polymer micelle geometry, and thereby identify any distinctions between simple and complex (FK) spherical phases, we looked first at the dimensionless Helmholtz free energy per monomer $F/k_{\mathrm{B}}T$, and volume-averaged polyhedral imprinting $\langle \alpha \rangle_V$, of metastable phases across phase space. Our goal with this initial approach to the large dataset was two-fold: first to verify the numerical reliability and consistency of our geometric calculations, and second to identify any immediately apparent features of the data including relationships of geometry with system parameters such as ϵ, χN, and f_{A}.

A representative sample from the dataset is shown in Fig. 3, with trends in free energy that are as expected from previous work [38]. The magnitude of imprinting is comparable to previous studies [27], albeit at different conditions here, inspiring confidence in our methods. Imprinting monotonically increases with f_{A}, which is also expected: as the core swells towards the cell boundaries, and the corona blocks shorten and become less flexible, the boundaries of the encapsulating Voronoi cell are more strongly imposed on the micelle core [23]. The thermodynamic implications of this swelling will be discussed in Sec. V. As is clear from Fig. 3, imprinting of the Voronoi cell polyhedra on the polymer micelle cores (the A/B interface) is significantly higher in the Frank-Kasper phases than in the simple particle-forming phases fcc and bcc. Note also that there are no crossovers, such that at a given state point the phases are always ordered bcc, fcc, σ, A15, from least to greatest

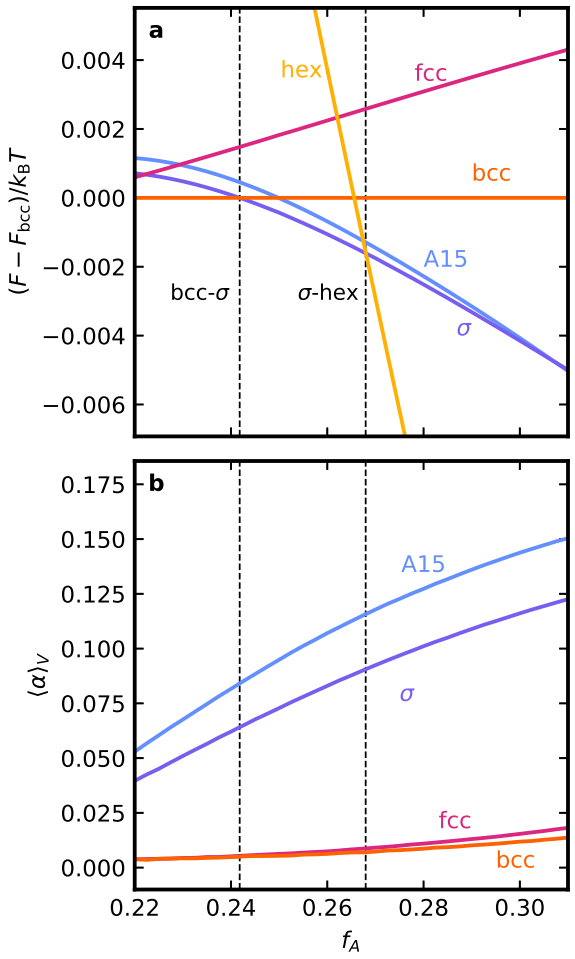


FIG. 3. (a) Dimensionless free energy relative to the bcc phase, and (b) volume-averaged polyhedral imprinting, versus block-fraction at $\epsilon = 1.8$ and $\chi N = 23$.

degree of imprinting. These relationships are consistent across the probed region of phase space, with the degree of imprinting of metastable bcc and fcc phases never approaching that of σ and A15, as demonstrated by additional data in the SM [41].

To further understand how micelle geometry evolves across phase space, we then examined the relationship between polyhedral imprinting $\langle\alpha\rangle_V$ and χN. As depicted in Fig. 4, at fixed f_A and ϵ, imprinting monotonically increases with χN for all candidate phases within the particle-forming region of phase space. It is well known that, in response to increases in χN, the A/B interface sharpens, exhibiting a steeper crossover of volume fractions ϕ_A and ϕ_B [43–45]. Based on this phenomenon alone, however, it is not clear whether one should expect imprinting to increase or decrease. One might reasonably expect either: a more imprinted

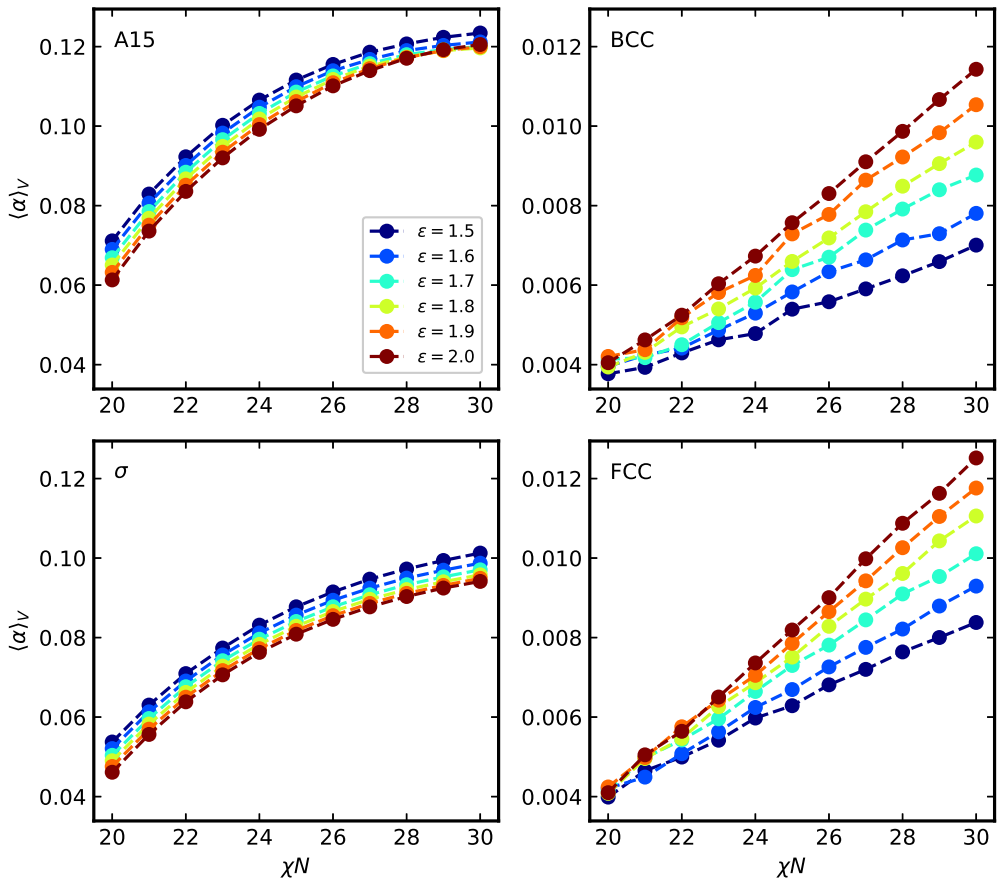


FIG. 4. Volume-averaged polyhedral imprinting versus the Flory-Huggins interaction parameter χN at $f_A = 0.25$, for ϵ increasing from dark blue to red. Note that the scale for $\langle\alpha\rangle_V$ is one order of magnitude smaller for the simple phases to better visualize the data.

interface would result from stricter constraints on corona chain configurations, but a more spherical interface would result from increased enthalpic penalties for interfacial area. The data support the former hypothesis, and the explanation, which will be discussed in Sec. V, requires more nuance than simply looking at interfacial area as in strong-segregation theory (SST) [25].

Perhaps most interesting in Fig. 4 is the effect of the conformational asymmetry, ϵ, on polyhedral imprinting. It is reasonable to expect increases in polyhedral imprinting with increasing ϵ, as the corona stiffens and imposes the boundaries of the Voronoi cell on the relatively more flexible core [6]. However, this intuition is not entirely born out in the data. While fcc and bcc do exhibit increases in imprinting with ϵ, the FK phases σ

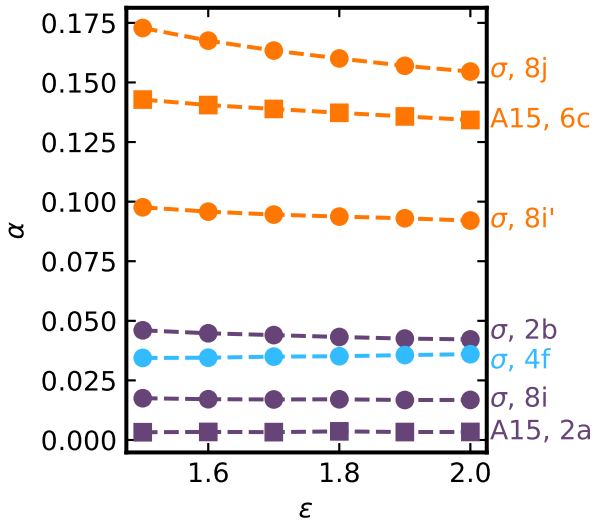


FIG. 5. Polyhedral imprinting versus ϵ for each particle type in σ (circles) and A15 (squares), at $\chi N = 25$ and $f_A = 0.25$. Orange lines correspond with Z14 polyhedra (14 faces), light blue ones with Z15 polyhedra, and dark purple ones with Z12 polyhedra.

and A15 display the opposite behavior: increasing ϵ leads to apparently lower polyhedral imprinting of the Voronoi polyhedra on the micelle core. This trend reversal is consistent with observations reported in the pioneering study of diblock copolymer spherical phase geometry by Reddy *et al.* [27]; their data for the A15 phase at $\chi N = 40$ and $f_A = 0.29$ exhibits a decrease in polyhedral imprinting with increasing conformational asymmetry, and shows that this decrease is primarily driven by the Z14 particles (Wyckoff position 6c). In addition to reproducing this behavior in A15 at different conditions, our calculations reveal a qualitatively identical trend in σ, thereby demonstrating a clear and presumably general contrast between the geometry of FK phases and fcc/bcc.

To test the limits of the geometric similarities between A15 and σ, we also examined the relationships between single-particle imprinting and ϵ. Because fcc and bcc each only have a single particle, trends of single-particle imprinting for these phases are implicit in Fig. 4. For the Frank-Kasper phases, we especially wanted to clarify whether average geometric changes in the system with ϵ were manifest in all particles, or driven by a few particles while others remained unchanged, as suggested by the A15 data in Ref. 27. Figure 5 reveals that the latter is the case. More specifically, Z14 particles in both σ and A15 exhibit by far the least spherical cores and are also responsible for shifts in imprinting with ϵ. The

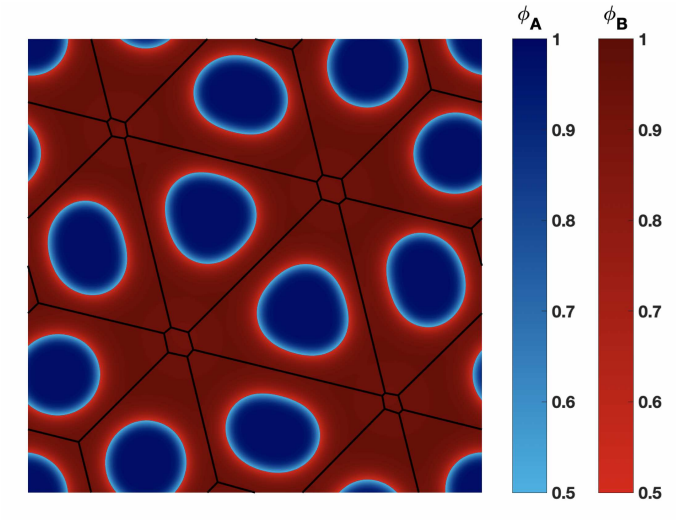


FIG. 6. The (001) plane of the σ volume-fraction fields ϕ_A (blue) and ϕ_B (red) at $\epsilon = 1.5$, $\chi N = 23$, $f_{\mathrm{A}} = 0.29$. The cross-section of the 3D Voronoi tessellation of the unit cell is indicated by the black lines. Wyckoff positions are labelled in white text within the figure.

distorted cores are also visible in the examples of Fig. 2b and Fig. 6. On the contrary, Z12 particles (colored dark purple) in σ and A15, and Z15 particles (colored light blue) in σ, are only slightly imprinted and exhibit a negligible change in response to increasing ϵ. The relationship, if any, between a particle's tendency to imprint and its coordination number is currently unclear, and more particle-forming phases would need to be analyzed to elicit an answer to this question.

Reddy *et al.* [27] explained the counterintuitive drop in the imprinting order parameter with increasing ϵ for Z14 cells in A15 by demonstrating that the micelle core geometry at low values of ϵ did not reflect a sphere being somewhat imprinted upon by the Voronoi polyhedron, but instead a discoidal shape that was somewhat flattened. They also observed a transition of the core from discoidal to faceted quasi-spherical with increasing ϵ. Because the discoidal core shape exhibits a higher surface area to volume ratio (lower IQ) than the faceted quasi-spherical core shape, this transition is accompanied by a decrease in the apparent imprinting. Our results suggest that this discoidal transition identified in A15 is also present in the σ phases; the distinction between discoidal and polyhedral core shapes is qualitatively illustrated by the (001) plane of the σ unit cell in Fig. 6. A discoidal core is apparent in Figs. 2 and 6 at Wyckoff position 8i′, while the core at Wyckoff position 4f is clearly faceted in Fig. 6. Though this polyhedron appears more faceted, α at position 4f

is less than at position 8i′ (Fig. 5). As ϵ increases (see SM [41]), the core at position 8i′ becomes subtly more faceted while α decreases.

IV. GEOMETRIC SHIFTS ACROSS THE BCC-σ TRANSITION

With a stronger understanding of the geometry of polymer micelles in metastable and stable classical and FK spherical phases, we now look explicitly at the changes in micelle geometry across the bcc-σ OOT. Keeping in mind that the average imprinting in a phase tends to be driven by only some of the symmetry-inequivalent particles, how does the average polyhedral character of the A/B interface (the micelle core) change across a phase transition? It is expected from the earlier analysis of metastable phases that there will be a geometric discontinuity at the bcc-σ transition. Figure 7 confirms this expectation by providing the imprinting of the equilibrium phase for varying conditions, and clarifies two important observations about the nature and magnitude of the change in imprinting.

First, the relationship between average imprinting and block fraction f_{A} appears pinned to the location of the phase transition, with trends that are shifted but nearly equivalent otherwise for different values of χN at fixed ϵ. This feature is seen more readily in Fig. 7b, where the abscissa origin has been shifted to the location of the OOT for each condition. Similar figures were generated for other values of ϵ, and are available in the SM [41]. It is remarkable that, though polymer micelle geometry varies with the system parameters, stability tracks this particular measure of micelle geometry across phase space, suggesting the two are closely and consistently related.

Second, the difference in imprinting, or imprinting gap, between σ and bcc at the phase transition is approximately constant with respect to χN. This is not a trivial result; there are points in phase space (for example, at low or high f_{A} in Fig. 3b) where the imprinting gap between metastable σ and bcc is significantly greater than or less than the gap at the OOT. However, the phase transitions are located at values of f_{A} with nearly identical gaps in imprinting. This phenomenon is more clearly illustrated in Fig. 8, which depicts the size of the imprinting gap across the bcc-σ phase boundary for varying system parameters. The imprinting gap decreases significantly with increasing ϵ, as can also be deduced from Fig. 4. In contrast, though clearly not constant, the imprinting gap decreases only slightly with χN. This second observation is closely tied to the first observation, and suggests that the

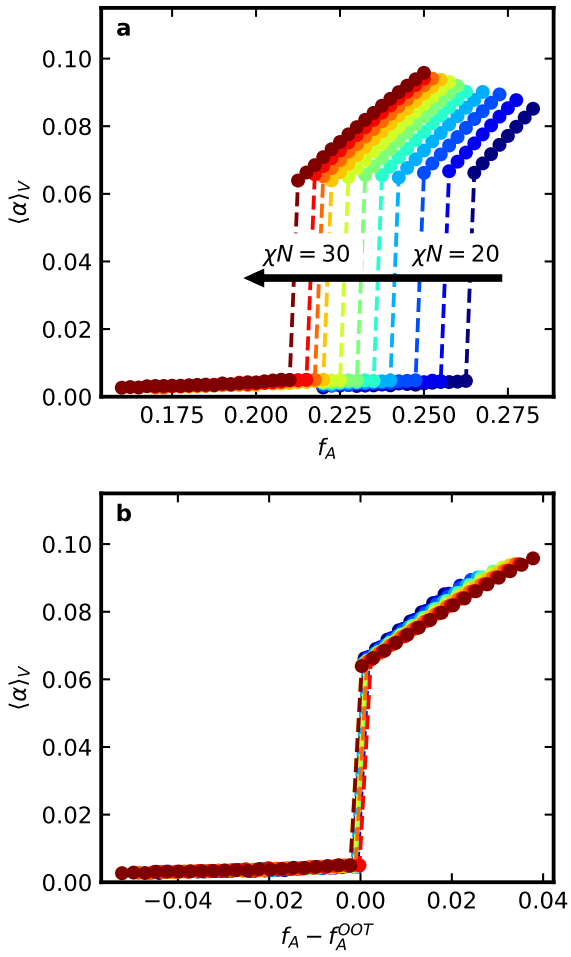


FIG. 7. Polyhedral imprinting of the equilibrium phase as a function of f_{A}, for varying χN at $\epsilon = 1.8$. (a) χN increases from dark blue to red, and the curve shifts left in accordance with the shift of the OOT. (b) The x-axis is shifted by the respective location of the bcc-σ OOT for each value of χN, leading to a near-collapse of the curves.

difference in micelle core geometry between σ and bcc is closely tied to the location of the order-order transition.

One way to think about phase stability from the standpoint of geometry is to cast the jump in imprinting at the bcc-σ OOT as a barrier to transitioning that must be overcome. This can be thought of as the micelles experiencing an increasing drive, or a squeeze, to deform as f_{A} increases [23], but being unable to deform while constrained to a bcc lattice. The transition is delayed due to resistance to deformation by the core block, which must assume a state of unequal stretching in a faceted quasi-spherical core. Once that drive to

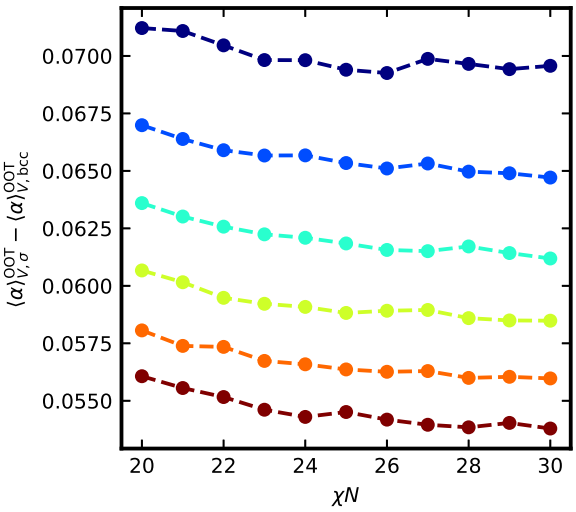


FIG. 8. The difference, or gap, in polyhedral imprinting between σ and bcc across the OOT as a function of χN for varying values of ϵ. Coloring is in accordance with Fig. 4, with ϵ increasing from 1.5 (dark blue) to 2.0 (red).

deform increases enough, however, the system accommodates the deformation while partially alleviating the resistance of the core to unequal stretching by transitioning to the σ phase, which has Voronoi polyhedra that are slightly more spherical than those in bcc. This rationalization properly accounts for the shift downwards of $f_{\mathrm{A}}^{\mathrm{OOT}}$ as ϵ increases, since this corresponds with increasing pliability of the core block relative to the corona block.

V. FREE ENERGY IMPLICATIONS OF POLYHEDRAL IMPRINTING

To more deeply explore this connection between phase stability and interfacial geometry, it was necessary to investigate the nature of the driving force for interface deformation. A common argument, first made by Lee *et al.* [6], for the stability of the Frank-Kasper phases focuses on the fact that their Wigner-Seitz cells are more spherical than those of fcc and bcc. They claim that the FK phases should better minimize distortion of the packed polymer micelles from the ideal spherical state they would exhibit in isolation. Though a good starting point, this argument does not fully capture the geometric and thermodynamic details of the exchange in stability between bcc and σ. To be specific, our SCFT calculations demonstrate that σ particle cores are actually universally more distorted than those of bcc, including at

the OOT (Fig. 3), suggesting that distortion of entire particles is not minimized in σ relative to bcc. What, then, is the thermodynamic driving force (and its physical manifestation) for the transition from σ to bcc?

To develop an argument that fully captures these details, we framed our geometric results in the context of the thermodynamics of particle-forming phases in diblock copolymer melts. We examined three distinct contributions to the free energy [25]: the enthalpic contribution due to unfavorable A/B interactions,

$$\frac{U}{k_{\mathrm{B}}T} = \frac{\chi}{V}\int_V \mathrm{d}\mathbf{r}\ \phi_{\mathrm{A}}(\mathbf{r})\,\phi_{\mathrm{B}}(\mathbf{r}), \tag{12}$$

and the individual entropic stretching penalties of A and B blocks,

$$-\frac{S_{\mathrm{A}}}{k_{\mathrm{B}}} = -\frac{1}{V}\int_V \mathrm{d}\mathbf{r}\ \frac{\rho_{\mathrm{J}}(\mathbf{r})}{N}\ln q(\mathbf{r},f) + \omega_{\mathrm{A}}(\mathbf{r})\,\phi_{\mathrm{A}}(\mathbf{r}) \tag{13}$$

$$-\frac{S_{\mathrm{B}}}{k_{\mathrm{B}}} = -\frac{1}{V}\int_V \mathrm{d}\mathbf{r}\ \frac{\rho_{\mathrm{J}}(\mathbf{r})}{N}\ln q^{\dagger}(\mathbf{r},f) + \omega_{\mathrm{B}}(\mathbf{r})\,\phi_{\mathrm{B}}(\mathbf{r}), \tag{14}$$

where ρ_{J} is the distribution of diblock junctions [25]. For the sake of simplicity, we do not discuss the contribution of the translational entropy of the A/B junctions. Note that because

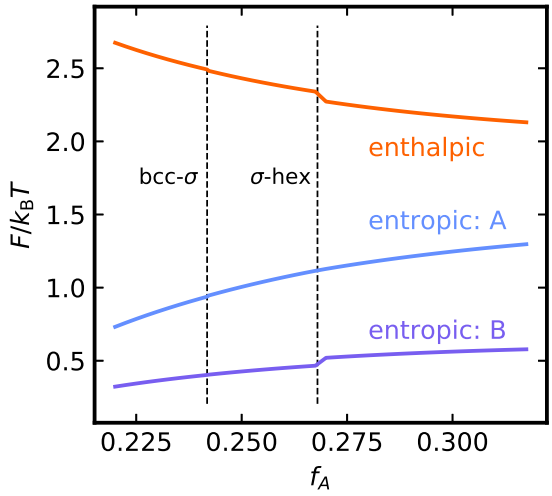


FIG. 9. Enthalpic interaction and entropic stretching contributions to the free energy of the equilibrium phase as a function of f_{A}, at $\epsilon = 1.8$ and $\chi N = 23$. The locations of order-order transitions are indicated by dashed lines. At the σ-hex transition, discontinuities in the contributions are apparent. At the bcc-σ transition, similar but much smaller discontinuities are present, and will be discussed later.

the system is incompressible, the internal energy and enthalpy are equivalent. We choose conventionally, but arbitrarily, to refer to the enthalpy with the symbol U. Also, note that the total free energy of Eq. (8) is shifted by a constant relative to that given in Ref. 25. The resulting enthalpic and entropic stretching contributions to the free energy are tracked as functions of f_{A} in Fig. 9, akin to results previously reported by Matsen and Bates [25].

Not surprisingly, stretching penalties for the core block monotonically increase with f_{A}. This is consistent with the fact that polyhedral imprinting of the A/B interface is also increasing (Fig. 3), which leads to non-uniform chain-stretching in the core [27, 46]. Despite assuming a more uniformly stretched state as the core becomes more polyhedral, corona block stretching penalties still monotonically increase with f_{A}, likely because stretching energy scales as N_{B}^{-1} [8]. More interestingly, enthalpic interactions decrease as f_{A} increases. Viewed through the lens of SST, this is a counterintuitive result [25]; in a strongly segregated system, the enthalpy is purely controlled by the interfacial area, which increases with f_{A}. However, in this intermediate-segregation system, crossovers from A-rich to B-rich regions may be gradual, leading to diffuse interfaces [25] that contribute significantly to the enthalpy integral of Eq. (12). Changes in the interface diffuseness thus make the details of the integration necessary to fully understand the trend in enthalpy, rather than relying solely on intuition from SST.

To test the extent to which changes in interfacial width are responsible for the downward trend in enthalpy, we separated the integral over the unit cell in Eq. (12) into three components defined by volume fraction boundaries: u_{core} ($\phi_{\mathrm{A}} > 0.75$), u_{corona} ($\phi_{\mathrm{A}} < 0.25$), and $u_{\mathrm{interface}}$ ($0.25 < \phi_{\mathrm{A}} < 0.75$),

$$u_{\mathrm{core}} = \frac{1}{V} \int_{V:\ \phi_A \in [0.75,\, 1.00]} \mathrm{d}\mathbf{r}\ \phi_{\mathrm{A}}(\mathbf{r})\, \phi_{\mathrm{B}}(\mathbf{r}) \tag{15}$$

$$u_{\mathrm{interface}} = \frac{1}{V} \int_{V:\ \phi_A \in [0.25,\, 0.75]} \mathrm{d}\mathbf{r}\ \phi_{\mathrm{A}}(\mathbf{r})\, \phi_{\mathrm{B}}(\mathbf{r}) \tag{16}$$

$$u_{\mathrm{corona}} = \frac{1}{V} \int_{V:\ \phi_A \in [0.00,\, 0.25]} \mathrm{d}\mathbf{r}\ \phi_{\mathrm{A}}(\mathbf{r})\, \phi_{\mathrm{B}}(\mathbf{r}) \tag{17}$$

where the cutoff values represent reasonable approximations for the boundaries of each region of the micelle. Figure 10 shows these components for three values of f_{A} at fixed χN and ϵ.

The interfacial contribution to the enthalpy integral increases with f_{A}, aligned with the results in the strong-segregation limit. Neither the core nor corona contributions on their

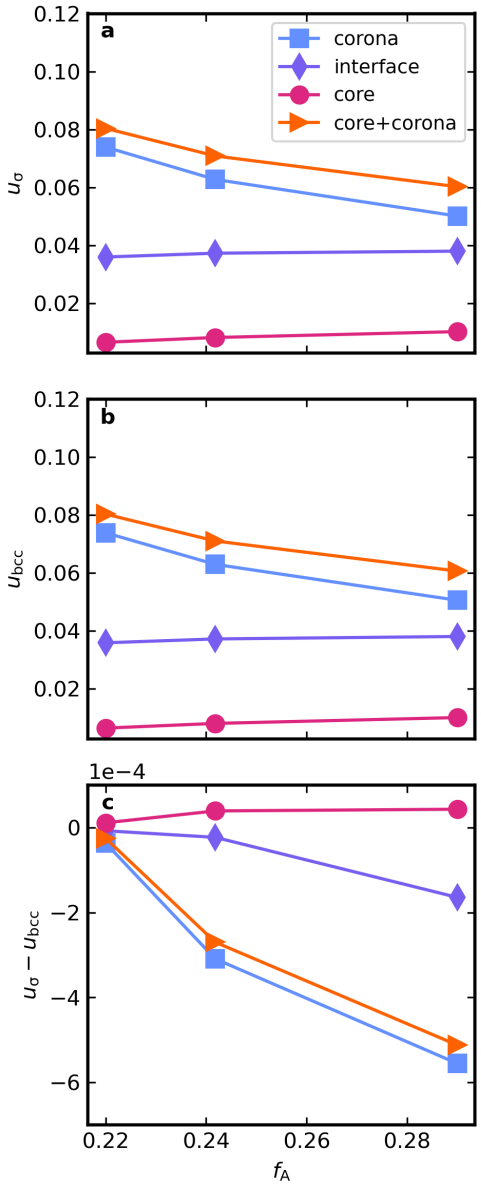


FIG. 10. Contributions to the enthalpy integral, given by Eqs. (15)-(17), for (a) σ and (b) bcc diblock copolymer melts at $\chi N = 23$ and $\epsilon = 1.8$. The difference in each contribution is given in panel (c). The "core+corona" contribution is the sum of Eqs. (15) and (17). The values of f_A were chosen to bracket the bcc-σ OOT at $f_A \approx 0.242$.

own shed any light on the issue, as changes in their composition are simultaneous with changes in their relative volumes, both affecting their enthalpic contribution. The core contribution to the enthalpy integral increases with f_A (its volume increases), while the corona contribution decreases (its volume decreases). However, their sum does decrease

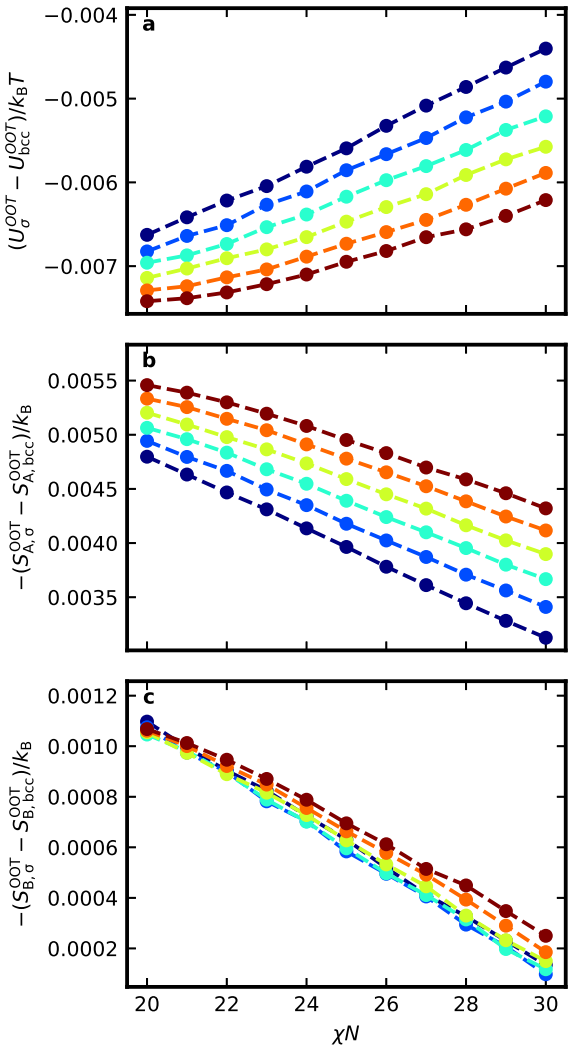


FIG. 11. Difference in each free energy contribution across the bcc-σ OOT with respect to χN. Coloring corresponds with increasing ϵ from dark blue to red, in accordance with Fig. 4 and Fig. 8.

with f_A, implying overall decrease of A/B contact in the core and corona. This suggests that, at identical state points, σ tends to exhibit less diffuse A/B interfaces than bcc, with less A/B contact in the core and corona overall. This insight from the enthalpy is confirmed visually upon examination of 1-D volume fraction profiles of bcc and σ, provided in the SM [41].

At the bcc-σ transition, the change in the interfacial contribution to the enthalpy is very small, as is clear in Fig. 10c, suggesting it contributes little to σ's preferential formation over

bcc. Instead, it is the decrease of the sum of the core and corona enthalpic contributions at the OOT, indicating sharpening of the interface, that drives the overall decrease in enthalpy with f_A. Notably, sharpening of the A/B interface is concurrent with increasing imprinting, which can be seen by comparing Figs. 3 and 10. This suggests a way to think about the evolution of the A/B interface: spherical interfaces tend to be wider and more diffuse, while imprinted interfaces tend to be sharper and more abrupt. The corresponding increases in entropic penalties suggest that this an effect of ordering. In the intermediate-segregation regime, then, ordering of the polymer chains and imprinting of the micelle core tends to offer a substantial enthalpic benefit through interface sharpening while coming at the cost of entropic stretching penalties.

We can apply this framework to better understand the order-order transition from bcc to σ. We examined the differences, or gaps, in each free energy contribution between σ and bcc at the OOT (Fig. 11). Upon transitioning from bcc to σ, polyhedral imprinting increases (Fig. 8), enthalpy decreases (Fig. 11a), entropic penalties for stretching of the core block increase (Fig. 11b), and entropic penalties for stretching of the corona block increase but less so than the core block (Fig. 11c). These trends are maintained at the OOT across the particle-forming region of phase space. Keeping in mind the perspective on interfacial width established by the previous paragraph, enthalpy (and thus imprinting) is the driving force for the transition from bcc to σ, while stretching penalties oppose the transition. What is stopping bcc micelles from imprinting more to reduce enthalpy, then? Each metastable phase's geometry reflects a local optimum in the free energy landscape that is a balance of the different contributions. This indicates that the resulting stretching penalties from further imprinting in bcc are too high, exceeding in magnitude the enthalpic benefits that would be reaped by sharpening the A/B interface. A reasonable explanation for this phenomenon is that the shape of the bcc Wigner-Seitz cells is not conducive to imprinting due to low sphericity, while the polyhedra in σ are more spherical, tying back into the generic arguments presented by Lee *et al.* [6]. This is consistent with the transition occurring earlier in f_A as χN increases, as penalties for diffuse interfaces increase and sharp interfaces are thus sooner and more strongly preferred.

VI. CONCLUDING REMARKS

This study provides clarity on the relationship between micelle geometry and thermodynamics of particle-forming intermediate-segregation diblock copolymer melts. We make no *ex-ante* approximations regarding segregation strength or interface shape. The results give way to an intuitive mechanistic understanding of the bcc-σ OOT, highlighting A/B interface narrowing, concurrent with core deformation, as the dominant force driving phase transition. We anticipate that, upon further investigation, these observations will also apply at the σ-A15 transition [21], where further increases in micelle core polyhedrality at the OOT will likely correspond with a similar reduction in enthalpy. It must be noted that the calculations were done in the mean-field limit, and thus neglect potentially impactful fluctuation effects that would be present in real materials [21]. Additionally, we have focused solely on conformationally asymmetric single-component diblock copolymer melts; considering other polymer systems constitutes an exciting route for future investigation. For the neat diblock copolymer melt, it may be interesting to consider conformationally symmetric systems in the hex stability region of the phase diagram, where prior work suggests a bcc-A15 transition [22], to see if the general principles elucidated here in the region of Frank-Kasper phase stability extends to these metastable systems. A more complex system, such as a copolymer/homopolymer blend with micellar particles swollen by core homopolymer [47–51], may exhibit different geometric and thermodynamic features near OOTs and coexistence windows. Furthermore, there is room to more thoroughly unpack the relationship, if any, between particle coordination and geometry. Nevertheless, the analysis developed here should facilitate a better understanding of the role of molecular structure in determining micelle geometry, and the relationship between local micelle geometry and overall phase stability.

ACKNOWLEDGMENTS

We recognize David C. Morse for valuable input on technical aspects of PSCF, as well as Frank S. Bates for additional discussion. We also recognize Nathan Stover for contributions to optimization of the code in Ref. 42. This work was supported by NSF Grant No. DMR-1719692. The Minnesota Supercomputing Institute at the University of Minnesota provided

computational resources used for this study.

---

[1] F. S. Bates, M. A. Hillmyer, T. P. Lodge, C. M. Bates, K. T. Delaney, and G. H. Fredrickson, Science **336**, 434 (2012).

[2] F. S. Bates and G. H. Fredrickson, Phys. Today **52**, 32 (1999).

[3] D. J. Kinning and E. L. Thomas, Macromolecules **17**, 1712 (1984).

[4] C. D. Han, N. Y. Vaidya, and D. Kim, Macromolecules **33**, 3767 (2000).

[5] J. Zhang, S. Sides, and F. S. Bates, Macromolecules **45**, 256 (2012).

[6] S. Lee, C. Leighton, and F. S. Bates, Proc. Natl. Acad. Sci. U.S.A. **111**, 17723 (2014).

[7] A. P. Lindsay, A. J. Mueller, M. K. Mahanthappa, T. P. Lodge, and F. S. Bates, Wigner-seitz cell generation and calculations in matlab, `https://hdl.handle.net/11299/223279` (2021).

[8] M. Doi and S. Edwards, *The Theory of Polymer Dynamics* (Oxford University Press, New York, NY, 1986).

[9] T. P. Lodge and P. C. Hiemenz, *Polymer Chemistry, Third Edition* (CRC Press, Boca Raton, FL, 2020).

[10] P. J. Flory, J. Chem. Phys. **10**, 51 (1942).

[11] L. Leibler, Macromolecules **13**, 1602 (1980).

[12] Y. Y. Huang, J. Y. Hsu, H. L. Chen, and T. Hashimoto, Macromolecules **40**, 406 (2007).

[13] N. W. Hsu, B. Nouri, L. T. Chen, and H. L. Chen, Macromolecules **53**, 9665 (2020).

[14] C. Zhang, D. L. Vigil, D. Sun, M. W. Bates, T. Loman, E. A. Murphy, S. M. Barbon, J.-A. Song, B. Yu, G. H. Fredrickson, A. K. Whittaker, C. J. Hawker, and C. M. Bates, J. Am. Chem. Soc. **143**, 14106 (2021).

[15] C. A. Tyler and D. C. Morse, Phys. Rev. Lett. **94**, 208302 (2005).

[16] M. Takenaka, T. Wakada, S. Akasaka, S. Nishitsuji, K. Saijo, H. Shimizu, M. I. Kim, and H. Hasegawa, Macromolecules **40**, 4399 (2007).

[17] M. W. Matsen and M. Schick, Phys. Rev. Lett. **72**, 2660 (1994).

[18] D. A. Hajduk, P. E. Harper, S. M. Gruner, C. C. Honeker, G. Kim, L. J. Fetters, and G. Kim, Macromolecules **27**, 4063 (1994).

[19] S. Lee, M. J. Bluemle, and F. S. Bates, Science **330**, 349 (2010).

[20] N. Xie, W. Li, F. Qiu, and A. C. Shi, ACS Macro Lett. **3**, 909 (2014).

[21] M. W. Bates, J. Lequieu, S. M. Barbon, R. M. Lewis, K. T. Delaney, A. Anastasaki, C. J. Hawker, G. H. Fredrickson, and C. M. Bates, Proc. Natl. Acad. Sci. U.S.A. **116**, 13194 (2019).

[22] G. M. Grason, B. A. DiDonna, and R. D. Kamien, Phys. Rev. Lett. **91**, 058304 (2003).

[23] G. M. Grason, Phys. Rep. **433**, 1 (2006).

[24] A. Reddy, X. Feng, E. L. Thomas, and G. M. Grason, Macromolecules **54**, 9223 (2021).

[25] M. W. Matsen and F. S. Bates, J. Chem. Phys. **106**, 2436 (1997).

[26] K. D. Dorfman, Macromolecules **54**, 10251 (2021).

[27] A. Reddy, M. B. Buckley, A. Arora, F. S. Bates, K. D. Dorfman, and G. M. Grason, Proc. Natl. Acad. Sci. U.S.A. **115**, 10233 (2018).

[28] J. K. Cockcroft, A Hypertext Book of Crystallographic Space Group Diagrams and Tables, `http://img.chem.ucl.ac.uk/sgp/mainmenu.htm`.

[29] P. D. Olmsted and S. T. Milner, Phys. Rev. Lett. **72**, 936 (1994).

[30] P. D. Olmsted and S. T. Milner, Macromolecules **31**, 4011 (1998).

[31] A. Arora, J. Qin, D. C. Morse, K. T. Delaney, G. H. Fredrickson, F. S. Bates, and K. D. Dorfman, Macromolecules **49**, 4675 (2016).

[32] A. Arora, D. C. Morse, F. S. Bates, and K. D. Dorfman, J. Chem. Phys. **146**, 244902 (2017).

[33] G. H. Fredrickson, *The Equilibrium Theory of Inhomogeneous Polymers* (Oxford University Press, New York, NY, 2006).

[34] R. B. Thompson, K. Rasmussen, and T. Lookman, J. Chem. Phys. **120**, 31 (2004).

[35] P. Stasiak and M. W. Matsen, Eur. Phys. J. E **34**, 110 (2011).

[36] E. W. Cochran, C. J. Garcia-Cervera, and G. H. Fredrickson, Macromolecules **39**, 2449 (2006).

[37] A. Ranjan, J. Qin, and D. C. Morse, Macromolecules **41**, 942 (2008).

[38] K. Kim, M. W. Schulze, A. Arora, R. M. Lewis, M. A. Hillmyer, K. D. Dorfman, and F. S. Bates, Science **356**, 520 (2017).

[39] M. De Graef and M. McHenry, *Structure of Materials* (Cambridge University Press, Cambridge, UK, 2007).

[40] G. Pólya, *Induction and Analogy in Mathematics* (Princeton University Press, Princeton, NJ, 1954).

[41] See Supplemental Material at [URL will be inserted by publisher] for additional data for Figs. 3, 6 and 7 at other values of ϵ and χN, along with methodology validation and explanations.

[42] `https://github.com/rpcollanton/polymer_sphericity` (2021).

[43] E. Helfand and Y. Tagami, J. Chem. Phys. **56**, 3592 (1972).

[44] E. Helfand and Y. Tagami, J. Chem. Phys. **57**, 1812 (1972).

[45] A. N. Semenov, Macromolecules **26**, 6617 (1993).

[46] F. S. Bates and G. H. Fredrickson, Annu. Rev. Phys. Chem. **41**, 525 (1990).

[47] M. Zhao and W. Li, Macromolecules **52**, 1832 (2019).

[48] A. J. Mueller, A. P. Lindsay, A. Jayaraman, T. P. Lodge, M. K. Mahanthappa, and F. S. Bates, ACS Macro Lett. **9**, 576 (2020).

[49] G. K. Cheong, F. S. Bates, and K. D. Dorfman, Proc. Natl. Acad. Sci. U.S.A. **117**, 16764 (2020).

[50] J. Xie and A. C. Shi, Giant **5**, 100043 (2021).

[51] B. R. Magruder and K. D. Dorfman, Soft Matter **17**, 8950 (2021).